which follows the underlying α and β phase distribution, therefore influences how much of each species is incorporated, leading to a barrier layer that is variably doped (see Fig. 6a).

Due to the very high V concentration in the beta phase, thermal oxidation of the latter can bring to the formation of highly doped TiO_2 responsible of optical transition at very high wavelength. Since in this case incorporation of V^{5+} or V^{4+} can occur, there are localized states close to the valence band edge that induce a shift toward more positive value of the flat band potential and thus explaining that the measured photocurrent becomes zero close to ~ 0.4 V vs Ag/AgCl. However, less doped phase containing lower amount of vanadium have a more negative flat band potential and thus while the contribution to the measured photocurrent is almost zero from V rich oxide, we start to see the contribution of the less doped oxide, whose flat band potential is around ~ −0.6 V vs Ag/AgCl as already reported for Al and V free TiO_2 NTs grown in the same conditions [51]. Notably, this assumption also explains the trend in the differential capacitance. The measured capacitance is the sum of contribution of two parallel capacitance, i.e. the one form the less doped TiO_2 and the one from the more doped TiO_2 (Fig. 6). The latter is expected to be higher due to the high doping level that makes the space charge region very thin. When the potential is shifted in the negative direction, the capacitance raises at least until the potential is higher than the flat band potential (depletion layer), but when as the Fermi level at the interface approaches the band edge levels, the capacity of the space charge layer becomes independent of the electrode potential because the Fermi level is pinned in the conduction band. In the meantime the same trend but shifted by the difference in the flat band potentials was observed. We also measure the contribution of the other parallel capacitance, associated with the less doped oxide, which becomes comparable with that of the other parallel capacitance (related to the more doped oxide) and thus we can appreciate it.

Photoelectrochemical results demonstrate that the NTs grown on Ti6Al4V possess localized electronic states within the band gap that facilitate charge transport through the nanostructured oxide. These findings are in good agreement with recent studies reporting that alloying elements in Ti-based substrates can significantly influence the electronic structure and photoelectrochemical behaviour of the resulting anodic oxides [28].

3.4. Electrochemical measurements

The insights obtained from the photoelectrochemical characterization provide a solid framework to interpret the electrochemical behaviour of both bare Ti6Al4V and NTs-modified surfaces in simulated physiological environments: Hanks' balanced salt solution (HBSS), representing normal biological conditions, and simulated inflammatory conditions solution (SICS), reproducing oxidative inflammatory environments, whose composition is reported in Table 1.

According to the EIS spectra (Fig. 7a, b, d and e), the NTs exhibit an overall impedance approximately more than one order of magnitude lower than that of the bare, chemically etched alloy in HBSS. This marked difference between NTs and bare samples is also observed under inflammatory conditions (SICS), where the oxide layer is exposed to highly oxidizing species such as H_2O_2. Moreover, the NTs display phase angles of approximately 40° in HBSS and 30° in SICS, compared to the higher phase values of the bare alloy. This behaviour is consistent with the enhanced electronic conduction through the nanostructured oxide. It should be noted that the lower impedance values observed for NTs in the EIS measurements should not be directly interpreted as reduced corrosion resistance. This behavior can be attributed to the high electrochemically active surface area of the nanotubular structure, which enhances interfacial charge transfer processes. In addition, the doped nature of the oxide, as suggested by the low-energy optical transitions, contributes to increased electronic conductivity compared to stoichiometric anatase. As a result, both anodic (oxide growth/repair) and cathodic (oxygen reduction) reactions can occur more readily at open circuit conditions without necessarily leading to material degradation. EIS spectra in Nyquist representation at the corresponding open circuit potential has been included in the Supporting Information (see Fig. S3)

The EIS spectra were modelled using appropriate equivalent electrical circuits (EECs). For the bare Ti6Al4V alloy, which is naturally covered by a thin air-grown passive oxide layer, the experimental data were satisfactorily fitted using a simple single time-constant circuit (Fig. 8a). This model consists of the electrolyte resistance (R_{el}) in series with a parallel combination of the polarization resistance ($R_{p_o l}$) and a constant phase element ($Q_{o\times}$), which accounts for the non-ideal capacitive behaviour of the passive oxide film.

A different equivalent circuit was adopted for the NTs-coated samples (Fig. 8b), reflecting the more complex structure of the anodic oxide layer. The proposed model comprises a constant phase element (Q_{tube}), which represents the non-ideal capacitive behaviour of the nanotube walls, arranged in parallel with a series between the R_{tube}, the electrolyte resistance inside the nanotubular channels, and a parallel (R_b Q_b), element attributed to the compact barrier oxide layer located at the bottom of the pores. The resulting fitting parameters are summarized in Table 4.

Polarization curves (Fig. 7c,f) reveal that, in SICS, the bare alloy undergoes a significant shift of E_{corr} toward more positive values (due to the presence of oxidative agents) accompanied by a decrease in both corrosion current density (i_{corr}) and passive current density (i_{pass}) compared with HBSS. In contrast, the NT-modified surfaces show significantly higher i_{corr} and i_{pass} relative to the bare substrate in both media. Moreover, the passive region of the polarization curve of the NTs is significantly reduced, as oxygen evolution begins at relatively low anodic potentials. This behaviour reflects the higher electronic conductivity of the nanotubular anodic oxide layer, which facilitates

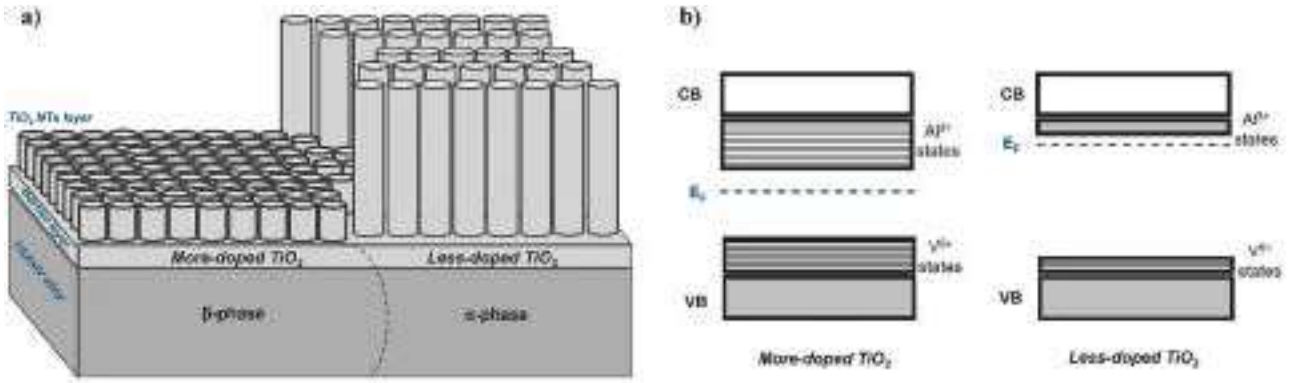

Fig. 6. a) Schematic illustration of the Ti6Al4V surface after anodization; b) Schematic representation of the band structure of oxide films grown on Ti6Al4V, illustrating donor (Al-related) and acceptor (V-related) defect states within the band gap and the position of the Fermi level E_F.

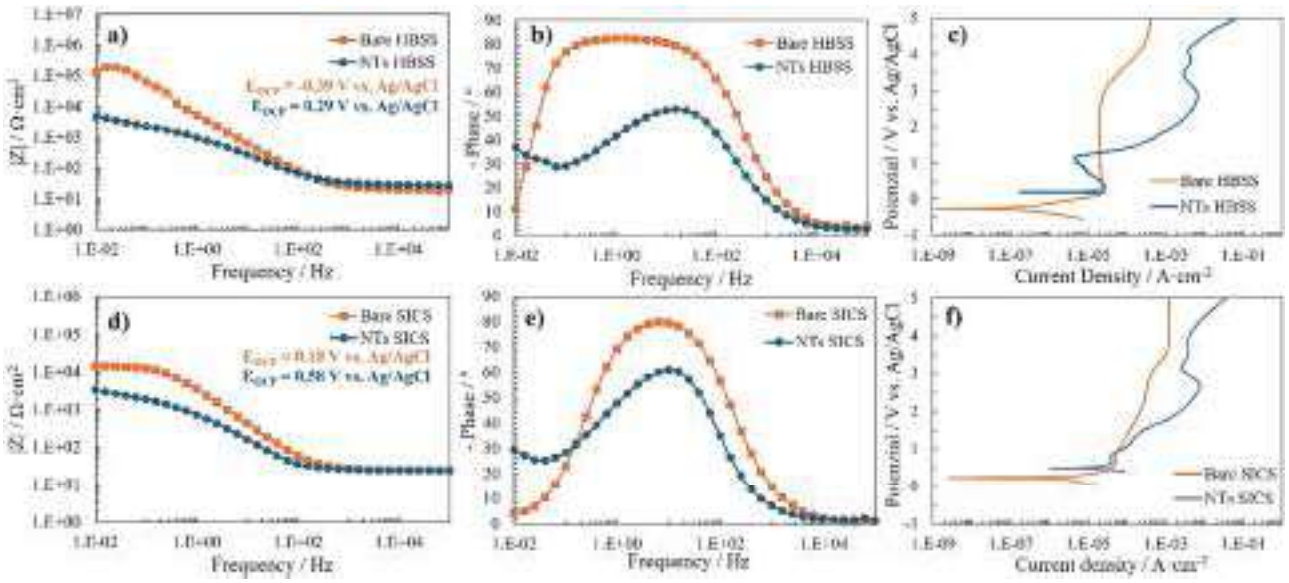

Fig. 7. EIS spectra in Bode representation (at corresponding open circuit potential E_{OCP}) and polarization curves related to bare Ti6Al4V and NTs grown on Ti6Al4V recorded in HBSS (a, b, c) and SICS (d, e, f).

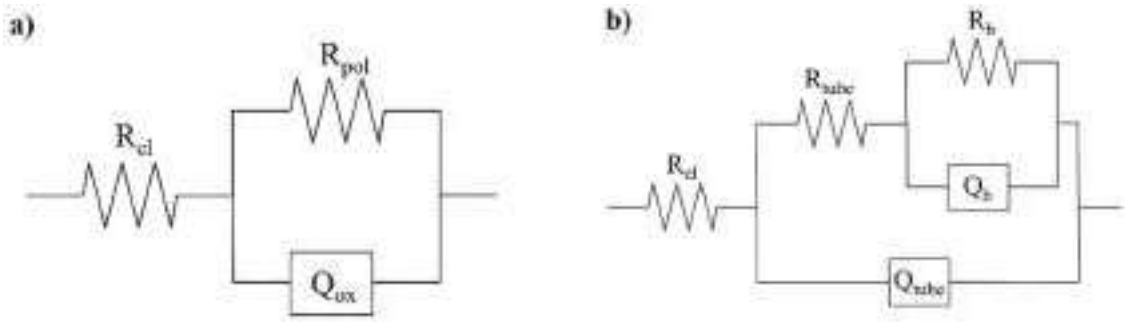

Fig. 8. Schematic representation of the equivalent electrical circuits used to model the EIS spectra shown in Fig. 7, for bare Ti6Al4V (a) and Ti6Al4V-NTs (b) in the two simulated solutions.

Table 4
Fitting parameters used to model the EIS spectra shown in Fig. 7, recorded for bare Ti6Al4V and Ti6Al4V-NTs in the two simulated solutions.

Sample	R_{el} / Ω cm^2	R_{pol} / Ω cm^2	Q_{ox} / F cm^{-2}	n	χ^2 max			
Bare HBSS	22.0 ± 1.3	$3.2{\cdot}10^5 \pm 8.6{\cdot}10^4$	$4.1{\cdot}10^{-5} \pm 2.0{\cdot}10^{-5}$	0.92 ± 0.06	$1.9{\cdot}10^{-2}$			
Bare SICS	23.0 ± 3.2	$1.4{\cdot}10^4 \pm 1.7{\cdot}10^3$	$5.5{\cdot}10^{-5} \pm 8.6{\cdot}10^{-6}$	0.93 ± 0.01	$1.1{\cdot}10^{-3}$			
Sample	**R_{el} / Ω cm^2**	**R_{tube}/ Ω cm^2**	**Q_{tube} / F cm^{-2}**	**n**	**R_b / Ω cm^2**	**Q_b / F cm^{-2}**	**n**	**χ^2 max**
NTs HBSS	28.6 ± 1.1	$1.8{\cdot}10^3 \pm 1.3{\cdot}10^2$	$1.8{\cdot}10^{-4} \pm 3.9{\cdot}10^{-6}$	0.72 ± 0.01	$1.2{\cdot}10^4 \pm 3.4{\cdot}10^3$	$1.2{\cdot}10^{-3} \pm 3.3{\cdot}10^{-4}$	0.53 ± 0.06	$2.2{\cdot}10^{-4}$
NTs SICS	21.6 ± 3.8	$8.3{\cdot}10^2 \pm 1.5{\cdot}10^2$	$1.5{\cdot}10^{-4} \pm 6.9{\cdot}10^{-5}$	0.87 ± 0.04	$1.1{\cdot}10^4 \pm 8.3{\cdot}10^2$	$9.3{\cdot}10^{-4} \pm 1.4{\cdot}10^{-5}$	0.38 ± 0.05	$1.7{\cdot}10^{-3}$

electrochemical reactions at the oxide–electrolyte interface and is consistent with the modifications in its electronic structure observed in the photoelectrochemical characterization.

It is noteworthy that for the NTs the corrosion potential (E_{corr}) in HBSS lies below the potential at which the photocurrent vanishes in the photocharacteristic curves ($E_{FB} \sim +0.4$ V vs Ag/AgCl). This implies that the anodic oxide operates under forward bias conditions, thereby exhibiting a less blocking, more conductive behaviour that promotes redox activity at the interface.

Taken together, these electrochemical results are fully consistent with the photoelectrochemical findings. The incorporation of Al^{3+} and V^{5+} into the oxide during anodization introduces localized donor and acceptor states, which enhance charge transport within the barrier layer. This modified electronic structure results in increased interfacial conductivity and explains the higher passive and corrosion currents, as well as the resistive EIS response, observed for the NTs in both HBSS and SICS.

3.5. *Hydroxyapatite growth*

Osteoinduction is the process by which stem cells differentiate into osteoblasts, promoting the regeneration of damaged bone tissue. This property depends on the bioactivity of the biomaterial, specifically its ability to form a hydroxyapatite (HA) layer when in contact with body fluids. HA [$Ca_{10}(OH)_2(PO_4)_6$], a calcium phosphate with a Ca/P ratio of 1.67, acts as a natural scaffold that supports cell adhesion, proliferation, and differentiation. Owing to its stability and excellent biocompatibility at physiological pH, HA provides ideal conditions for bone growth. To

replicate the physiological environment in vitro, simulated body fluids such as HBSS are commonly used.

To assess surface bioactivity, Ti6Al4V substrates with TiO_2 nanotube (NTs) arrays were immersed in HBSS solution for 28 days. SEM analysis of the surfaces (Fig. 9a-d) revealed a substantial transformation compared to the as-prepared implants. A homogeneous mineral layer uniformly covered the entire surface: characteristic "mud" structure is visible, consisting of a cracked layer of corrosion products [57–59]. Fig. S4 shows the NTs cross-sections after the immersion in HBSS solution. EDX analysis confirmed the presence of Na, Mg, Cl, C, and O (from the HBSS medium), along with a significant increase of Ca and P corresponding to a calcium phosphate coating (see Fig. 9e). Raman spectroscopy further confirmed the presence of HA, with characteristic ν_1 symmetric stretching (P–O) at 960 cm^{-1} (see Fig. 9f) [60].

The high conductivity of TiO_2 NTs enhances localized electrochemical reactions that induce surface alkalinization, thereby accelerating HA formation and providing a bioactive, osteoconductive interface. The less blocking character of the NTs array grown on Ti6Al4V alloy leads to oxygen reduction reaction, that occurs in a confined environment (the pore of the NTs) inducing a local alkalinization. The local alkalinization inside the nano-pores promote the formation and precipitation of HA, see Eqs (6-8) [61].

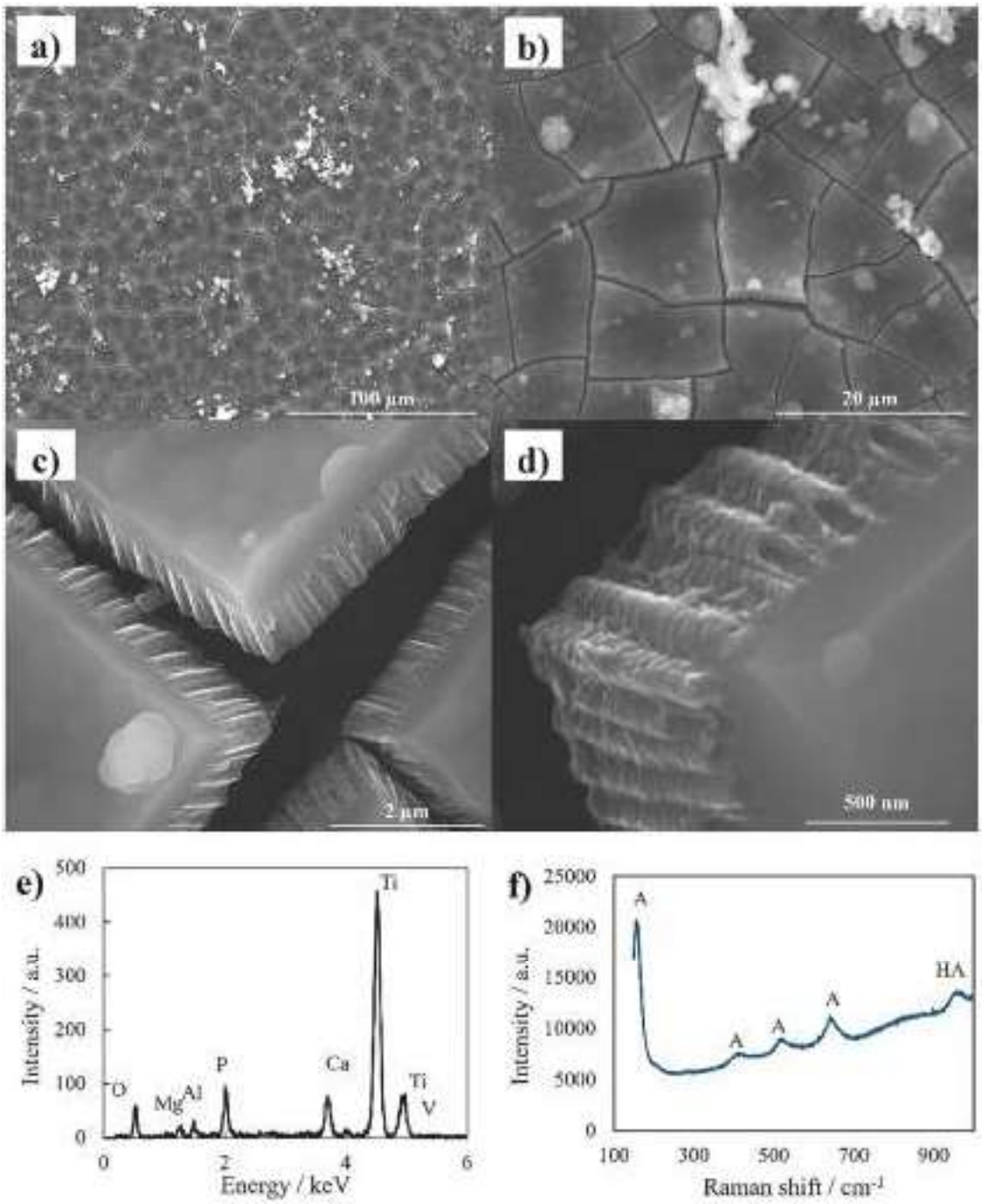

Fig. 9. Characterization of TiO_2 nanotube (NTs) samples after 28 days of immersion in HBSS: (a–d) SEM micrographs at different magnifications showing surface morphology and precipitate formation; (e) EDX elemental analysis performed on the NTs surface, corresponding to the area shown in Fig. 9b; (f) Raman spectrum confirming the presence of anatase (A) and hydroxyapatite (HA) phases on the NTs surface.

$$O_2 + 4e^- + 2H_2O \rightarrow 4OH^- \quad (6)$$

$$10Ca^{2+} + 8OH^- + 6HPO_4^{2-} \rightarrow Ca_{10}(PO_4)_6(OH)_2 + 6H_2O \quad (7)$$

$$10Ca^{2+} + 2OH^- + 6PO_4^{3-} \rightarrow Ca_{10}(PO_4)_6(OH)_2 \quad (8)$$

The consumption of phosphate ions due to HA precipitation shifts the dissociation equilibrium of HPO_4^{2-} toward PO_4^{3-}, thereby promoting their replenishment.

Although Hanks' solution is a buffered electrolyte and does not exhibit measurable pH variations in the bulk, local alkalinization cannot be excluded at the nanotube/electrolyte interface . In particular, the pH can change by several units within a very short time (on the order of seconds) due to half-cell reactions that produce or consume H^+ ions (in this work H^+ is consumed due to the oxygen reduction reaction) according to non-stationary Fick's law [62]. This effect is expected to be even more pronounced in the present system (even under open circuit conditions), where mass transport is hindered by the confined geometry of the NTs.

The confined microenvironment of the NTs pores contributes to a rapid and uniform mineralization process, supporting the potential of

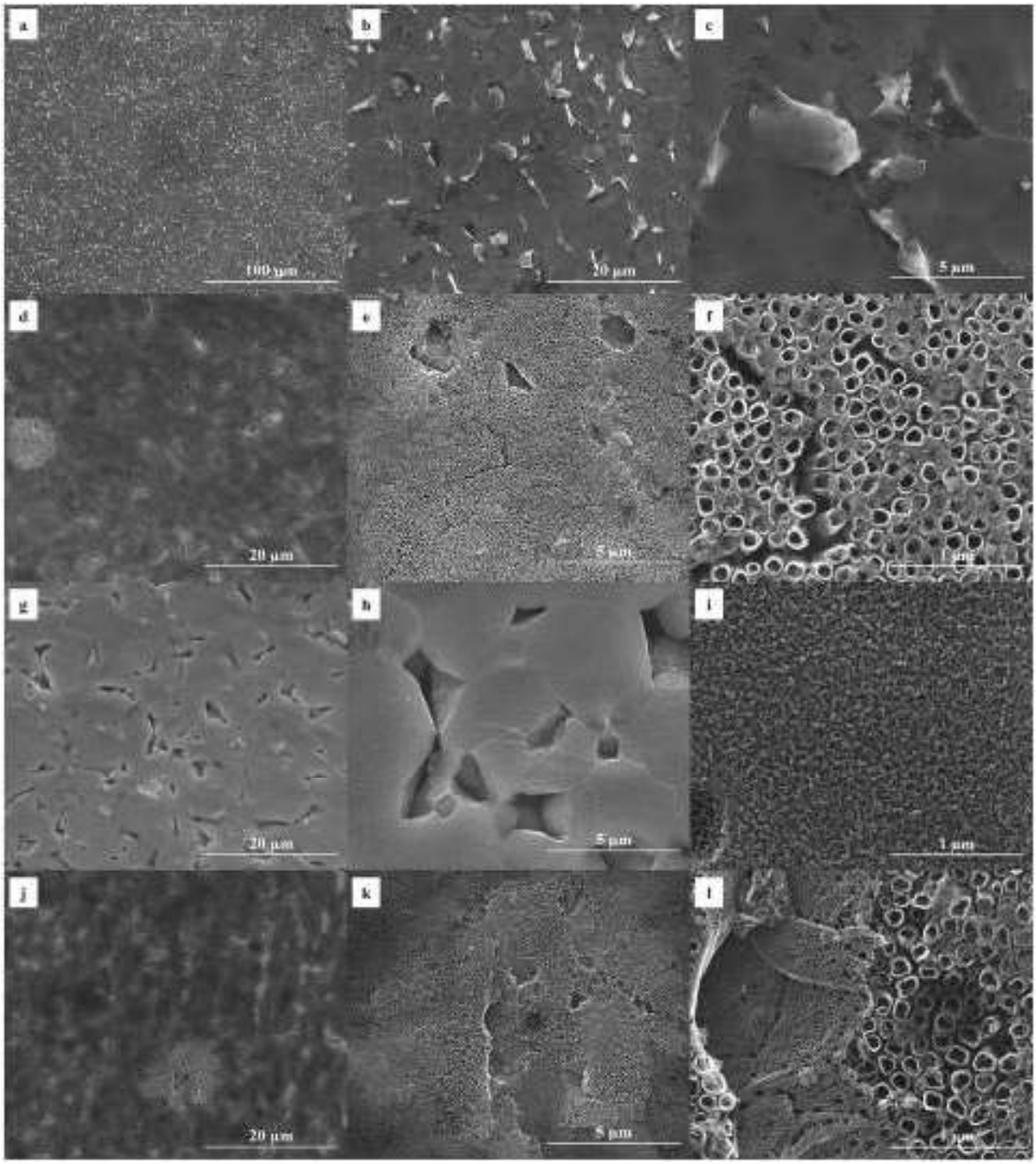

Fig. 10. SEM micrographs of samples after 168 h of immersion at 37 °C: a-b-c) Bare Ti6Al4V in HBSS, d-e-f) NTs in HBSS, g-h-i) Bare Ti6Al4V in SICS, j-k-l) NTs in SICS.

NT-modified Ti6Al4V implants for improved osseointegration because the HA layer observed on the NTs can provide a bioactive interface that promotes direct bone fixation without the need for bone cement.

Positively charged calcium ions first bind to the negatively charged Ti–OH groups on the surface. Then, phosphate (PO_4^{3-}) and carbonate (CO_3^{2-}) ions attach to the adsorbed calcium, forming a Ca/P-rich layer that gradually crystallizes into bone-like apatite [15]. This crystallization is enhanced by the surface's high energy, microporosity, and irregularities, which promote ion nucleation [63]. Moreover, hydroxyapatite formation proceeds faster when driven by ion exchange between the surface and the simulated body fluid [15].

3.6. Immersion tests and ions release evaluation

To evaluate the corrosion resistance of the modified surfaces under inflammatory-like conditions, long-term immersion tests were performed in HBSS and SICS at 37 °C for 168 h, reproducing both physiological and severe inflammatory environments. These tests mimic the early post-implantation inflammatory phase, typically lasting about one week, and simulate the oxidative stress conditions where reactive oxygen species (ROS) such as hydrogen peroxide and free radicals are produced by immune cells.

During inflammation, leukocytes release highly reactive species, including H_2O_2, HO•, and HO_2• radicals, that can compromise the stability of the protective TiO_2 layer. When coupled with mechanical stresses, this process can trigger the release of metallic ions and detachment of nanoscale debris, leading to the accumulation of corrosion products in surrounding tissues. Such phenomena can aggravate the inflammatory response and, in severe cases, contribute to implant loosening or failure.

SEM analysis revealed no significant morphological differences between the bare Ti6Al4V surface before immersion (Fig. 1) and after 168 h in HBSS (Fig. 10a–c) and the surface maintained its characteristic α + β microstructure. For the NT-modified samples, immersion in HBSS resulted in the formation of small surface deposits containing Mg, Ca, and P, indicative of early calcium phosphate precipitation, while the overall nanotubular morphology remained intact (Fig. 10d–f). These findings confirm that both bare and anodized samples exhibit good stability in HBSS, with no significant degradation. In contrast, pronounced differences were observed under SICS exposure. Bare Ti6Al4V surfaces exhibited selective dissolution of the β-phase, resulting in the initiation of micro-pits and cracks along β-phase boundaries (Fig. 10g–i). This preferential attack is consistent with literature reports showing that the β-phase, enriched in vanadium, displays lower corrosion resistance in oxidative environments, leading to localized thinning and oxide-induced stress corrosion cracking [5,64]. Moreover, a slight increase in roughness was observed locally on the α-phase, where nanoporous features appeared, leading to a mildly more textured surface (Fig. 10i).

In contrast, TiO_2 nanotube (NTs) surfaces maintained their structural integrity even after 168 h of immersion in SICS. The nanotube morphology remained well-defined, with no evidence of collapse or detachment (Fig. 10j-l). These results demonstrate that the NTs act as a robust and stable barrier, minimizing direct exposure of the alloy substrate to the aggressive solution and preventing localized dissolution.

ICP-OES results confirmed the morphological observations. The concentrations of Ti, Al, and V detected in the HBSS solutions were negligible for both sample types, indicating good chemical stability in neutral conditions (quantitative data are reported in Supporting Information, Fig. S5).

In contrast, under SICS exposure, ICP-OES analysis showed that ions release from NTs samples was lower than that from the bare alloy at all immersion times. The calculated average values of released ions are reported in Table 5 and Fig. 11. In particular, after 168 h of immersion in SICS at 37 °C, the NTs-modified samples reduced the release of Ti, Al, and V by 47.4%, 57.9%, and 52.6%, respectively, compared to the bare alloy.

Table 5
The average concentration values and standard deviation (μg·cm^{-2}) of metallic ions released into SICS solution at 37 °C after different immersion times (n = 3).

Sample	Immersion time / h	Concentration of metallic ions / μg·cm^{-2}		
		Ti	Al	V
Bare SICS	24	31.8 ± 18.8	2.22 ± 1.9	4.9 ± 3.5
	72	79.0 ± 23.9	5.3 ± 3.3	13.7 ± 9.2
	168	173.0 ± 4.6	11.9 ± 4.2	31.4 ± 18.4
NTs SICS	24	34.5 ± 2.6	5.0 ± 0.9	8.1 ± 2.8
	72	129.7 ± 20.9	13.5 ± 3.8	29.1 ± 11.5
	168	328.8 ± 37.6	28.3 ± 8.1	66.2 ± 23.58

The relatively high vanadium concentration detected in SICS solutions for bare samples supports the hypothesis of preferential β-phase dissolution, in agreement with SEM findings. In contrast, the absence of selective β-phase dissolution in nanotubular surfaces under conditions specifically designed to promote it highlights their potential in mitigating phase-dependent degradation mechanisms.

It should be noted that the trends observed in ion release do not always directly correlate with polarization resistance (R_p), as discussed in Section 3.4. While R_p reflects instantaneous interfacial electrochemical processes, ICP-OES measurements account for the cumulative material dissolution over time. In the simulated inflammatory environment, dissolution is governed not only by electrochemical processes but also by chemically assisted mechanisms. In particular, oxidative species (H_2O_2) and complexing agents (e.g., lactic acid) can enhance metal ion solubilization independently of the electrochemical response.

During inflammatory conditions, reactive oxygen species are generated through enzymatic pathways. The oxidizing environment simulated by SICS, containing 150 mM H_2O_2, is more aggressive than typical physiological conditions but it was intentionally selected to represent a worst-case scenario and to accelerate degradation processes within experimentally accessible times. Indeed, milder conditions have been reported in the literature, such as 0.1% H_2O_2 in PBS [65], or 150 mM H_2O_2 at moderately acidic pH (≈5.2)) [30]. Therefore, the present results should be interpreted as a comparative and mechanistic assessment under highly oxidative conditions, and caution should be taken when extrapolating them directly to clinical scenarios.

During such conditions, vanadium ions can catalyze Fenton-like reactions with hydrogen peroxide, producing highly reactive radicals that further accelerate oxide degradation according to the following reaction:

$$V^{2+}\left(V^{3+},\ V^{4+}\right) + H_2O_2 \rightarrow V^{3+}\left(V^{4+}, V^{5+}\right) + OH^{\bullet} + OH^{-} \quad (9)$$

This reaction mechanism mirrors the well-established Fenton chemistry of iron and has also been described for other transition metals, including titanium [5,66].

Indeed, the equilibrium potentials for the V^{3+}/V^{4+} and V^{4+}/V^{5+} redox couples are 0.28 and 0.48 V vs. SHE, respectively, according to the Pourbaix diagram [36]. These values are more cathodic than the equilibrium potential of the H_2O_2/OH• couple, which is 1.025 V at pH 2 [67]. Therefore, the proposed mechanism is thermodynamically feasible.

The resulting hydroxyl and hydroperoxyl radicals intensify local oxidative stress, perpetuating the inflammatory cycle: the inflammatory environment promotes metal ion release, while the released ions catalyze further ROS production, thus creating a self-sustaining feedback loop.

Overall, the combined morphological and ICP-OES analysis demonstrates that TiO_2 nanotube surfaces mitigate the potential biological risks associated with vanadium and aluminium release under inflammatory conditions.

4. Conclusions

The bimodal α + β microstructure of Ti6Al4V leads to distinct

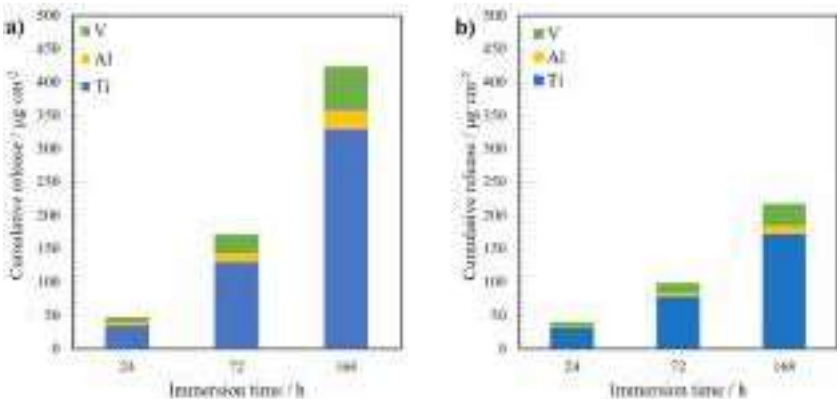

Fig. 11. Mean cumulative release of Ti, Al, and V determined by ICP–OES for (a) chemically etched (bare) Ti6Al4V and (b) NT–modified Ti6Al4V samples after 168 h immersion in SICS at 37 °C.

behaviours during anodization, resulting in heterogeneous nanotube formation. Nanotube layers form predominantly over the α-phase, while the β-phase exhibits a more porous oxide without a well-defined nanostructure.

Photoelectrochemical analysis revealed that the TiO_2 nanotube arrays possess localized electronic states within the mobility gap, enhancing electronic conduction through the nanostructured oxide. This improved conductivity contributes to localized electrochemical reactions, which are relevant for both corrosion resistance and hydroxyapatite formation.

Long-term immersion tests combined with EIS and ICP-OES measurements demonstrated that NT-modified surfaces exhibit superior corrosion resistance compared to bare Ti6Al4V. SEM analysis confirmed that the morphology of the NTs remained largely unchanged after 168 h in simulated inflammatory conditions (SICS), whereas bare samples showed preferential dissolution of the β-phase. Cumulative ions release from NTs was approximately one order of magnitude lower than from bare samples, highlighting the protective effect of the nanotube layer against alloying element leaching.

HA precipitation tests further showed that NT surfaces effectively promote apatite formation. Raman spectroscopy confirmed the presence of hydroxyapatite, and SEM images revealed dense, well-adhered mineral layers that fill the nanotube pores. The high surface area, nanoscale porosity, and conductive properties of NTs accelerate local alkalinization and HA nucleation, suggesting that osseointegration can be facilitated without additional coatings.

Overall, Ti6Al4V substrates modified with TiO_2 nanotube arrays demonstrate enhanced bioactivity, improved corrosion resistance, and reduced ion release, providing a multifunctional surface that supports both mechanical stability and biological integration. These findings indicate that NT-modified implants have significant potential for long-term clinical applications, combining favourable electrochemical performance with accelerated bone-bonding capability.

Funding

M.L.L. acknowledges the European Union (NextGeneration EU), for funding PhD Scholarship.

Data availability

Data available on request from the authors.

Declaration of competing interest

The authors declare that they have no known competing financial interests or personal relationships that could have appeared to influence the work reported in this paper.

Supplementary materials

Supplementary material associated with this article can be found, in the online version, at doi:10.1016/j.electacta.2026.148936.

References

[1] Q. Chen, G.A. Thouas, Metallic implant biomaterials, Mater. Sci. Eng. R: Rep. 87 (2015) 1–57, https://doi.org/10.1016/j.mser.2014.10.001.
[2] A. Thakur, A. Kumar, S. Kaya, R. Marzouki, F. Zhang, L. Guo, Recent advancements in surface modification, characterization and functionalization for enhancing the biocompatibility and corrosion resistance of biomedical implants, Coatings 12 (2022), https://doi.org/10.3390/coatings12101459.
[3] R. Davis, A. Singh, M.J. Jackson, R.T. Coelho, D. Prakash, C.P. Charalambous, W. Ahmed, L.R.R. da Silva, A.A. Lawrence, A comprehensive review on metallic implant biomaterials and their subtractive manufacturing, Int. J. Adv. Manuf. Technol. 120 (2022) 1473–1530, https://doi.org/10.1007/s00170-022-08770-8.
[4] A. Bandyopadhyay, I. Mitra, S.B. Goodman, M. Kumar, S. Bose, Improving biocompatibility for next generation of metallic implants, Prog. Mater. Sci. 133 (2023), https://doi.org/10.1016/j.pmatsci.2022.101053.
[5] M. Prestat, D. Thierry, Corrosion of titanium under simulated inflammation conditions: clinical context and in vitro investigations, Acta Biomater. 136 (2021) 72–87, https://doi.org/10.1016/j.actbio.2021.10.002.
[6] N. Eliaz, Corrosion of metallic biomaterials: a review, Mater. (Basel) 12 (2019), https://doi.org/10.3390/ma12030407.
[7] A. Kumar, G. Singh, Surface modification of Ti6Al4V alloy via advanced coatings: mechanical, tribological, corrosion, wetting, and biocompatibility studies, J. Alloys Compd (2024) 989, https://doi.org/10.1016/j.jallcom.2024.174418.
[8] C. Leyens, M. Peters, Titanium and Titanium Alloys : Fundamentals and Applications, Wiley, 2006.
[9] S. Kannan, C. Pugalendhi, B. Purushothaman, A.H. Seikh, R. Nallaiyan, Hopes on europium-coated titanium nanotubes and their opportunities in extra calcification, Surf. Coat. Technol (2024) 481, https://doi.org/10.1016/j.surfcoat.2024.130620.
[10] P. Bocchetta, L.Y. Chen, J.D.C. Tardelli, A.C. Dos Reis, F. Almeraya-Calderón, P. Leo, Passive layers and corrosion resistance of biomedical ti-6al-4v and β-ti alloys, Coatings 11 (2021), https://doi.org/10.3390/coatings11050487.
[11] J. Kim, H. Lee, T.S. Jang, D. Kim, C.B. Yoon, G. Han, H.E. Kim, H.Do Jung, Characterization of titanium surface modification strategies for osseointegration enhancement, Met. (Basel) (2021) 11, https://doi.org/10.3390/met11040618.
[12] V. Jordanovová, M. Losertová, M. Štencek, T. Lukášová, G.S. Martynková, P. Peikertová, Microstructure and properties of nanostructured coating on Ti6Al4V, Mater. (Basel) 13 (2020), https://doi.org/10.3390/ma13030708.
[13] V.K. Manivasagam, R.M. Sabino, P. Kantam, K.C. Popat, Surface modification strategies to improve titanium hemocompatibility: a comprehensive review, Mater. Adv. 2 (2021) 5824–5842, https://doi.org/10.1039/d1ma00367d.
[14] F. Zamparini, C. Prati, L. Generali, A. Spinelli, P. Taddei, M.G. Gandolfi, Micro-nano surface characterization and bioactivity of a calcium phosphate-incorporated titanium implant surface, J. Funct. Biomater. 12 (2021), https://doi.org/10.3390/jfb12010003.
[15] P. Prochor, Ż.A. Mierzejewska, Bioactivity of PEEK GRF30 and Ti6Al4V SLM in simulated body fluid and hank's balanced salt solution, Mater. (Basel) 14 (2021), https://doi.org/10.3390/ma14082059.
[16] A.M. Castillo-Paz, K.V. García-Vazquez, D.F. Cañon-Davila, M.A. Hernandez-Landaverde, L.H. Chan-Chan, R. Ramírez-Bon, M.E. Rodriguez-Garcia, In vitro immersion study and characterization of biomimetic bovine hydroxyapatite scaffolds: influence of calcination temperature (600 and 1000 °C) on apatite formation, Ceram. Int. 50 (2024) 26949–26962, https://doi.org/10.1016/j.ceramint.2024.04.426.

[17] L. Jacquot, M.P. Bonnin, A. Machenaud, J. Chouteau, M. Saffarini, J.P. Vidalain, Clinical and radiographic outcomes at 25-30 years of a hip stem fully coated with hydroxylapatite, J. Arthroplasty 33 (2018) 482–490, https://doi.org/10.1016/j.arth.2017.09.040.

[18] B.E. Nagay, J.M. Cordeiro, V.A.R. Barao, Insight into corrosion of dental implants: from biochemical mechanisms to designing corrosion-resistant materials, Curr. Oral Health Rep. 9 (2022) 7–21, https://doi.org/10.1007/s40496-022-00306-z.

[19] L.C. Campanelli, C.C. Bortolan, P.S.C.P. da Silva, C. Bolfarini, N.T.C. Oliveira, Effect of an amorphous titania nanotubes coating on the fatigue and corrosion behaviors of the biomedical Ti-6Al-4V and Ti-6Al-7Nb alloys, J. Mech. Behav. Biomed. Mater. 65 (2017) 542–551, https://doi.org/10.1016/j.jmbbm.2016.09.015.

[20] J. Grotberg, A. Hamlekhan, A. Butt, S. Patel, D. Royhman, T. Shokuhfar, C. Sukotjo, C. Takoudis, M.T. Mathew, Thermally oxidized titania nanotubes enhance the corrosion resistance of Ti6Al4V, Mater. Sci. Eng. C 59 (2016) 677–689, https://doi.org/10.1016/j.msec.2015.10.056.

[21] S. Ahmadi, I. Mohammadi, S.K. Sadrnezhaad, Hydroxyapatite based and anodic Titania nanotube biocomposite coatings: fabrication, characterization and electrochemical behavior, Surf. Coat. Technol. 287 (2016) 67–75, https://doi.org/10.1016/j.surfcoat.2015.12.062.

[22] L. Benea, A. Ravoiu, V. Neaga, E.R. Axente, Using applied electrochemistry to obtain nanoporous TiO2 films on Ti6Al4V implant alloys and their preclinical In vitro characterization in biological solutions, Coatings 13 (2023), https://doi.org/10.3390/coatings13030614.

[23] S. De Santis, R. Varricchio, A. Ceccucci, G. Sotgiu, A. Di Masi, G. Magna, S. Sennato, M. Orsini, Cerium coatings on pristine and nanostructured Ti and Ti6Al4V surfaces: bioactivity, resistance in simulated inflammatory conditions, and antibacterial performance, ACS Biomater. Sci. Eng. 9 (2023) 3262–3272, https://doi.org/10.1021/acsbiomaterials.2c01461.

[24] K.A. Kumar Raju, A. Biswas, Corrosion behavior of self-organized TiO2 nanotubular arrays grown on Ti6Al4V for biomedical applications, Mater. Chem. Phys. 305 (2023), https://doi.org/10.1016/j.matchemphys.2023.128011.

[25] M. Slemnik, Comparative evaluation of corrosion resistance of AISI 316L and Ti6Al4V dental materials under simulated inflammatory conditions, Mater. (Basel) 18 (2025), https://doi.org/10.3390/ma18102243.

[26] N.F.E. Boraei, M.A.M. Ibrahim, S.S.A. El Rehim, I.H. Elshamy, Electrochemical corrosion behavior of β-Ti alloy in a physiological saline solution and the impact of H2O2 and albumin, J. Solid State Electrochem. 28 (2024) 2243–2256, https://doi.org/10.1007/s10008-023-05751-z.

[27] S. Yuan, J. Zou, N. Lin, H. Zhang, D. Li, Y. Wu, Understanding the protective role of a gradient titanium oxide ceramic layer on Ti6Al4V against corrosion via analyses of Mott-Schottky curve and electron work function (EWF), Ceram. Int. 48 (2022) 31896–31901, https://doi.org/10.1016/j.ceramint.2022.07.123.

[28] F. Di Franco, A. Zaffora, D. Pupillo, L. Iannucci, S. Grassini, M. Santamaria, The effect of electronic properties of anodized and hard anodized Ti and Ti6Al4V on their reactivity in simulated body fluid, J. Electrochem. Soc. 169 (2022) 071506, https://doi.org/10.1149/1945-7111/ac8316.

[29] A. Fonseca-García, J. Pérez-Alvarez, C.C. Barrera, J.C. Medina, A. Almaguer-Flores, R.B. Sánchez, S.E. Rodil, The effect of simulated inflammatory conditions on the surface properties of titanium and stainless steel and their importance as biomaterials, Mater. Sci. Eng. C 66 (2016) 119–129, https://doi.org/10.1016/j.msec.2016.04.035.

[30] S. Bahrampour, A. Bordbar-Khiabani, M. Hossein Siadati, M. Gasik, M. Mozafari, Improving the inflammatory-associated corrosion behavior of magnesium alloys by Mn3O4 incorporated plasma electrolytic oxidation coatings, Chem. Eng. J. 483 (2024), https://doi.org/10.1016/j.cej.2024.149016.

[31] F. Yu, O. Addison, A.J. Davenport, A synergistic effect of albumin and H2O2 accelerates corrosion of Ti6Al4V, Acta Biomater. 26 (2015) 355–365, https://doi.org/10.1016/j.actbio.2015.07.046.

[32] A. Bordbar-Khiabani, M. Gasik, Electrochemical and biological characterization of Ti–Nb–Zr–Si alloy for orthopedic applications, Sci. Rep 13 (2023), https://doi.org/10.1038/s41598-023-29553-5.

[33] A. Kityk, P. Švec, J. Šoltys, V. Pavlik, M. Hnatko, Deep inside of the mechanism of electrochemical surface etching of α + β Ti6Al4V alloy in room-temperature deep eutectic solvent Ethaline, J. Mol. Liq. 375 (2023), https://doi.org/10.1016/j.molliq.2023.121316.

[34] C. Sit Tig, M. Textor, N.D. Spencer, I.E. Land, P.-H. Vallotton, Surface characterization of implant materials c.p. Ti Ti-6Al-7Nb Ti-6Al-4V differ, Pretreat. (1999).

[35] E. Vermesse, C. Mabru, L. Arurault, Surface integrity after pickling and anodization of Ti-6Al-4V titanium alloy Open Archive Toulouse Archive Ouverte (OATAO) Surface integrity after pickling and anodization of Ti-6Al-4V titanium alloy, Appl. Surf, Sci. 285 (2013) 629–637, https://doi.org/10.1016/j.apsusc.2013.08.103ï.

[36] M. Pourbaix. Atlas of Electrochemical Equilibria in-Aqueous solutions, Pergamon Press Ltd, 1966.

[37] M.M. Lohrengel, A review Journal thin anodic oxide layers on aluminium and other valve metals: high field regime, 1993.

[38] P. Roy, S. Berger, P. Schmuki, TiO2 nanotubes: synthesis and applications, Angew, Chem, Int, Ed 50 (2011) 2904–2939, https://doi.org/10.1002/anie.201001374.

[39] R. Elaish, M. Curioni, K. Gowers, A. Kasuga, H. Habazaki, T. Hashimoto, P. Skeldon, Effects of fluoride ions in the growth of barrier-type films on aluminium, Electrochim. Acta 245 (2017) 854–862, https://doi.org/10.1016/j.electacta.2017.06.034.

[40] M.R. Arora, R. Kelly, Some Aspects of the Anodic Oxidation of V, Mo and W Y, J. Electrochem. Soc. 24 (1977).

[41] A.P. Simon, B. Lemes da Silva, E. Francescon Belusso, T.S. Mazzucatto, J. Soares Santos, F. Trivinho-Strixino, M. de Souza Sikora, Synthesis of bioactive TiO2 nanotubular thin films: exploring biocompatibility and biocorrosion behavior in simulated body environments, Surf. Coat. Technol. 474 (2023), https://doi.org/10.1016/j.surfcoat.2023.130077.

[42] U. Balachandran, N.G. Eror, Raman spectra of titanium dioxide, 1982.

[43] Y.J. Wu, C.Y. Wang, H. Mana-ay, C.S. Tu, P.L. Lai, P.Y. Chen, Achieving high surface bioactivity and adhesion in Ti-6Al-4V alloy via anodic oxidation and electrophoretic deposition, Ceram. Int. 51 (2025) 22755–22765, https://doi.org/10.1016/j.ceramint.2025.01.146.

[44] B. Ribeiro, R. Offoiach, E. Rahimi, E. Salatin, M. Lekka, L. Fedrizzi, On growth and morphology of tio2 nanotubes on ti6al4v by anodic oxidation in ethylene glycol electrolyte: influence of microstructure and anodization parameters, Mater. (Basel) 14 (2021), https://doi.org/10.3390/ma14102540.

[45] M. İzmir, B. Ercan, Anodization of titanium alloys for orthopedic applications, Front. Chem. Sci. Eng. 13 (2019) 28–45, https://doi.org/10.1007/s11705-018-1759-y.

[46] E. Matykina, A. Conde, J. De Damborenea, D.M.Y. Marero, M.A. Arenas, Growth of TiO2-based nanotubes on Ti-6Al-4V alloy, Electrochim. Acta 56 (2011) 9209–9218, https://doi.org/10.1016/j.electacta.2011.07.131.

[47] B. Ribeiro, R. Offoiach, S. Rossetti, E. Salatin, M. Lekka, L. Fedrizzi, On growth and morphology of TiO2 nanotubes on CP-Ti by anodic oxidation in ethylene glycol electrolyte: influence of electrolyte aging and anodization parameters, Mater. (Basel) 15 (2022), https://doi.org/10.3390/ma15093338.

[48] M. Sepúlveda, J. Capek, K. Baishya, J. Rodriguez-Pereira, J. Bacova, S. Jelinkova, R. Zazpe, H. Sopha, T. Rousar, J.M. Macak, Enhancement of biocompatibility of anodic nanotube structures on biomedical Ti–6Al–4V alloy via ultrathin TiO2 coatings, Front. Bioeng. Biotechnol. 12 (2024), https://doi.org/10.3389/fbioe.2024.1515810.

[49] A. Zaffora, F. Di Franco, F. Di Quarto, R. Macaluso, M. Mosca, H. Habazaki, M. Santamaria, The effect of Nb incorporation on the electronic properties of anodic HfO 2, ECS J. Solid State Sci. Technol. 6 (2017) N25–N31, https://doi.org/10.1149/2.0121704jss.

[50] M. Santamaria, G. Conigliaro, F. Di Franco, F. Di Quarto, Photoelectrochemical evidence of Cu2O/TiO2Nanotubes hetero-junctions formation and their Physicochemical characterization, Electrochim. Acta 144 (2014) 315–323, https://doi.org/10.1016/j.electacta.2014.07.154.

[51] C.M. Pecoraro, F. Di Franco, V. Loddo, M. Bellardita, M. Santamaria, Photoelectrolysis of glucose and fructose containing solution in PGM-free cells for hydrogen and valuable chemicals production, Int. J. Hydrog. Energy 87 (2024) 1277–1287, https://doi.org/10.1016/j.ijhydene.2024.09.124.

[52] M. Santamaria, G. Conigliaro, F. Di Franco, B. Megna, F. Di Quarto, Electronic properties of thermal oxides on Ti and their influence on impedance and photoelectrochemical behavior of TiO 2 nanotubes, J. Electrochem. Soc. 164 (2017) C113–C120, https://doi.org/10.1149/2.0601704jes.

[53] R.P. Lynch, A. Ghicov, P. Schmuki, A photo-electrochemical investigation of self-organized TiO_2 nanotubes, J. Electrochem. Soc. 157 (2010) G76, https://doi.org/10.1149/1.3276455.

[54] F. La Mantia, H. Habazaki, M. Santamaria, F. Di Quarto, A critical assessment of the Mott-Schottky analysis for the characterisation of passive film-electrolyte junctions, Russ. J. Electrochem. 46 (2010) 1306–1322, https://doi.org/10.1134/S102319351011011X.

[55] F. Di Quarto, F. Di Franco, S. Miraghaei, M. Santamaria, F.La Mantia, The amorphous semiconductor Schottky barrier approach to study the electronic properties of anodic films on Ti, J. Electrochem. Soc. 164 (2017) C516–C525, https://doi.org/10.1149/2.0551709jes.

[56] F. Di Quarto, F. La Mantia, M. Santamaria, Physicochemical characterization of passive films on niobium by admittance and electrochemical impedance spectroscopy studies, Electrochim. Acta (2005) 5090–5102, https://doi.org/10.1016/j.electacta.2005.03.065.

[57] V. Verro, F. Di Franco, D. Pupillo, M. Santamaria, A semiempirical model for predicting magnesium alloy biodegradation in simulated body fluids: influence of electrolyte composition and implant geometry, Electrochim. Acta 550 (2026), https://doi.org/10.1016/j.electacta.2025.148093.

[58] A. Cusanno, A. Rizzuti, A. De Bonis, D. Pupillo, M. Curcio, D. Sorgente, M. Santamaria, P. Mastrorilli, G. Palumbo, Pulsed laser deposition and phosphate chemical conversion coatings for tailoring the corrosion behavior of AZ31 resorbable implants manufactured via superplastic forming, Metall. Mater. Trans. B: Process Metall. Mater. Process. Sci. 57 (2026) 363–375, https://doi.org/10.1007/s11663-025-03849-5.

[59] H. Dong, F. Lin, A.R. Boccaccini, S. Virtanen, Corrosion behavior of biodegradable metals in two different simulated physiological solutions: comparison of Mg, Zn and Fe, Corros. Sci. 182 (2021), https://doi.org/10.1016/j.corsci.2021.109278.

[60] V.V. Nosenko, A.M. Yaremko, V.M. Dzhagan, I.P. Vorona, Y.A. Romanyuk, I. V. Zatovsky, Nature of some features in Raman spectra of hydroxyapatite-containing materials, J. Raman Spectrosc. 47 (2016) 726–730, https://doi.org/10.1002/jrs.4883.

[61] D. Pupillo, A. Zaffora, F. Di Franco, P. Picone, D. Nuzzo, M. Santamaria, Enhancing biocompatibility and antibacterial activity of Ti6Al4V by entrapping Ag and hydroxyapatite inside alginate filled pores of TiO2 layer grown by spark anodizing, Adv. Mater. Interfaces 10 (2023), https://doi.org/10.1002/admi.202201725.

[62] M. Santamaria, L. Asaro, P. Bocchetta, B. Megna, F. Di Quarto, Anodic electro deposition of CeO 2 and Co-doped CeO 2 thin films, J. Electrochem, Soc 160 (2013) D212–D217, https://doi.org/10.1149/2.065306jes.

[63] B. Makurat-Kasprolewicz, A. Ossowska, Recent advances in electrochemically surface treated titanium and its alloys for biomedical applications: a review of

anodic and plasma electrolytic oxidation methods, Mater, Today Commun. 34 (2023), https://doi.org/10.1016/j.mtcomm.2023.105425.
[64] F. Yu, O. Addison, A.J. Davenport, A synergistic effect of albumin and H2O2 accelerates corrosion of Ti6Al4V, Acta Biomater. 26 (2015) 355–365, https://doi.org/10.1016/j.actbio.2015.07.046.
[65] A. Sotniczuk, J.L. Gilbert, Y. Liu, M. Matczuk, W. Chromiński, D. Kalita, M. Pisarek, H. Garbacz, Corrosion resistance of β-phase titanium alloys under simulated inflammatory conditions: exploring the relevance of biocompatible alloying elements, Corros. Sci. 220 (2023), https://doi.org/10.1016/j.corsci.2023.111271.
[66] J. Prousek, Fenton chemistry in biology and medicine, in: Pure and Applied Chemistry, 2007, pp. 2325–2338, https://doi.org/10.1351/pac200779122325.
[67] Y. Nosaka, A. Nosaka, Understanding hydroxyl radical (•OH) generation processes in photocatalysis, ACS. Energy Lett. 1 (2016) 356–359, https://doi.org/10.1021/acsenergylett.6b00174.